



Designing visible-light optical coherence tomography towards clinics

Xiao Shu^{1#}, Lisa Beckmann^{1#}, Yuanbo Wang², Ian Rubinoff¹, Katie Lucy³, Hiroshi Ishikawa³, Gadi Wollstein³, Amani A. Fawzi⁴, Joel S. Schuman³, Roman V. Kuranov^{1,2}, Hao F. Zhang^{1,4}

¹Department of Biomedical Engineering, Northwestern University, Evanston, IL, USA; ²Opticent Health, Evanston, IL, USA; ³NYU Langone Eye Center, NYU School of Medicine, New York, NY, USA; ⁴Department of Ophthalmology, Northwestern University, Chicago, IL, USA

[#]These authors contributed equally to this work.

Correspondence to: Hao F. Zhang. Department of Biomedical Engineering, Northwestern University, Evanston, IL, USA.
Email: hfzhang@northwestern.edu.

Background: The capabilities of visible-light optical coherence tomography (vis-OCT) in noninvasive anatomical and functional retinal imaging have been demonstrated by multiple groups in both rodents and healthy human subjects. Translating laboratory prototypes to an integrated clinical-environment-friendly system is required to explore the full potential of vis-OCT in disease management.

Methods: We developed and optimized a portable vis-OCT system for human retinal imaging in clinical settings. We acquired raster- and circular-scan images from both healthy and diseased human eyes.

Results: The new vis-OCT provided high-quality retinal images of both subjects without any known eye diseases and patients with various retinal diseases, including retinal occlusive disease and diabetic retinopathy (DR) over a broad range of ages.

Conclusions: A newly designed vis-OCT system is sufficiently optimized to be suited for routine patients' examinations in clinics. Vis-OCT has the potential to add new anatomical and functional imaging capabilities to ophthalmic clinical care.

Keywords: Optical coherence tomography (OCT); high resolution imaging; ophthalmology

Submitted Feb 21, 2019. Accepted for publication May 04, 2019.

doi: 10.21037/qims.2019.05.01

View this article at: <http://dx.doi.org/10.21037/qims.2019.05.01>

Introduction

Optical coherence tomography (OCT) revolutionized ophthalmology in both fundamental investigations and clinical care by noninvasively providing high-resolution, three-dimensional (3D), *in vivo* optical biopsy of the eye (1-3). Since its introduction in 1991, a number of technologies were developed to broaden the application of OCT beyond structural imaging. Doppler OCT revealed axial blood flow velocity in retinal vessels (4-6), while polarization-sensitive OCT mapped the depolarization properties within multiple retinal layers (7,8). Recently, OCT angiography (OCTA) challenged traditional dye-based

fluorescence angiography as a non-invasive alternative with additional advantage in 3D imaging and has been applied to investigate almost all major blinding diseases (9-11).

Visible-light optical coherence tomography (vis-OCT) is a new technical extension of OCT, whose unique capabilities in structural and functional imaging have been demonstrated by several research groups (12-17). Exploiting shorter illumination wavelengths than the majority of OCT systems using near-infrared (NIR) light, vis-OCT offers significantly improved axial resolution using comparable spectral bandwidth (15,18). It has been shown that a 1.2- μm axial resolution in air (0.87- μm in tissue) can be achieved using a visible light source centered at 555 nm with a full-

width-at-half-maximum (FWHM) spectrum bandwidth of 156 nm, which can reveal tissue structure details at sub-micrometer level (14). A similar resolution can also be attained using an NIR light source centered at 785 nm yet with a FWHM bandwidth of 249 nm, which poses much greater challenges to the optical components and dispersion compensation in the system (19). Shorter wavelength can also improve lateral resolution of retinal imaging due to increased numerical aperture (NA), where the incident beam diameter is limited by the eye pupil.

In addition to the resolution advantage, vis-OCT offers increased absorption and scattering contrasts in biological tissues, at the cost of reduced penetration depth (14,20). The strong optical absorption of hemoglobin within the visible spectral range enabled accurate quantification of total hemoglobin concentration (21). Moreover, the attenuation spectrum of blood between 500 and 600 nm, once extracted through spectroscopic OCT analysis, can be fit against those of fully oxygenated and deoxygenated blood, which are much more distinctive in the visible-light spectral range than in the NIR spectral range, to determine oxygen saturation (sO_2) levels (12,21,22).

Furthermore, by combining *in vivo* arterial and venous sO_2 measurements with blood flow rates quantified by Doppler OCT several metabolic parameters can be calculated, including total oxygen delivery, oxygen extraction fraction (OEF), and metabolic rate of oxygen (MRO_2) (13,23-25). Since optical scattering of major biomolecules are larger in the visible than in the NIR spectral range (26), higher scattering contrast can be generated using the same illumination power in vis-OCT than using NIR-OCT (20). Finally, sub-resolution tissue abnormalities such as damages in retinal nerve fiber layer (RNFL) are detected more efficiently in the visible backscattering spectrum (27,28).

Rodent experiments have demonstrated that vis-OCT is an effective tool in ophthalmic research through metabolic and hemodynamic imaging of diseased rodent models. Liu *et al.* used vis-OCT to longitudinally monitor genetically modified type-1 diabetic mice (Akita/+, TSP1^{-/-}) and obtained metabolic parameters to compare with control mice (TSP1^{-/-}). The study suggested that increased OEF and MRO_2 precede microvascular alterations in diabetic retinopathy (DR) (29). Soetikno *et al.* applied vis-OCT to study a rat model of retinopathy of prematurity and found 59% decrease in inner retinal MRO_2 by postnatal day 18 (30). Besides using the absorption contrast in the visible spectrum range to calculate sO_2 and retinal MRO_2 , it was also demonstrated that vis-OCT can detect the

backscattering spectral difference between glaucomatous and healthy rodent eyes (12).

The promising results from rodents motivated the translation of vis-OCT to human applications. Yi *et al.* developed the first free-space vis-OCT system for human retinal imaging and demonstrated that the acquired OCT images had exceptional axial resolution. In the outer retinal layers, stronger scattering contrast from RNFL was demonstrated in comparison with NIR-OCT images taken by a commercial machine (31). In a follow-up study, Chen *et al.* quantified sO_2 in retinal blood vessels in healthy human subjects and showed significant oxygenation difference in different branches of retinal arteries and veins (32). The capabilities of vis-OCT in human retinal imaging were also demonstrated by Chong *et al.*, who developed a fiber-based system on an ophthalmoscope platform and reported less-than-2- μ m axial resolution. The study presented further measurements of blood flow velocity and sO_2 in retinal vessels by Doppler and spectroscopic analysis respectively (33).

Although these initial studies successfully demonstrated the capabilities of vis-OCT in obtaining structural and functional information of human retina, only images from healthy volunteers have been reported so far. It remains unclear whether vis-OCT can be applied to routine patient imaging for a few reasons. First, due to the lack of effective broadband optical amplifiers in the visible-light spectral range, current vis-OCT systems predominantly use supercontinuum (SC) lasers, whose high relative intensity noise leads to lower system sensitivity than the shot-noise-limited commercial NIR-OCT systems utilizing superluminescent or wavelength tunable lasers (swept-source) as a spatially coherent broadband light source. Second, the laser safety threshold for ocular imaging is more strict in the visible-light spectral range than in the NIR spectral range (34). Third, due to higher scattering, the human cornea and lens have lower transmission for visible than for NIR light and aging can further reduce lens transmission of visible light, which potentially affects the image quality of aged eyes (35,36). Fourth, the human retina is sensitive to visible light, which poses a challenge to eye fixation during vis-OCT image acquisition.

In this study, we report the development of a newly-designed vis-OCT clinical system for human retinal imaging. We designed a fiber-based interferometer and optimized optical designs for improved imaging signal-to-noise ratio (SNR). We also added a light emitting diode (LED) array for fellow-eye fixation. We imaged both

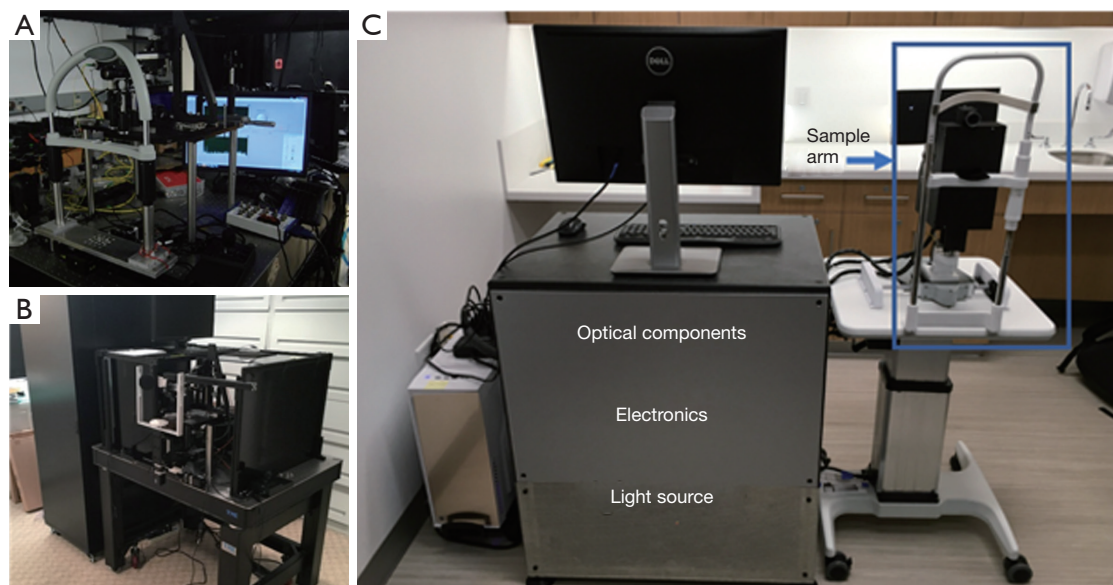


Figure 1 Evolution of human vis-OCT systems. (A) Photo of the laboratorial prototype system reported in Ref. (29); (B) photo of the engineering prototype system reported in Ref. (30); (C) photo of the latest clinical system with LED array mounted for fellow-eye fixation. Optical components, electronics, and the light source are all stored within the cart. Vis-OCT, visible-light optical coherence tomography; LED, light emitting diode.

volunteers without any known eye diseases and patients over a broad range of ages to demonstrate the image qualities of this newly-developed vis-OCT system.

Methods

Human subject recruitment

Our studies are approved by the Northwestern University Institutional Review Board and adhered to the tenets of the Declaration of Helsinki. We recruited both volunteers and patients with retinal vascular occlusive diseases and DR between 20 and 80 years of age. We obtained informed consent from all the subjects before their participations. Contact lenses and intraocular lenses were allowed but eyeglasses were requested to be removed. The uncorrected refractive errors of the imaged eyes ranged between +2 and -6 diopters. All patients underwent pupil dilation as part of their routine eye examinations. Some volunteers were imaged without dilation.

Imaging system

After demonstrating the first proof-of-concept prototype in 2015 (31), we integrated and packaged the breadboard-

based system to better adapt to the clinical environment, as shown in *Figure 1A,B* (32). However, operating the bulky system built on an optical table was still challenging for imaging technicians without engineering background.

In order to increase the user-friendly experience, to reduce operation complexity, and thus to facilitate clinical application, we developed a new portable vis-OCT system on an ophthalmic table, similar to the common commercial clinical eye imaging devices, as shown in *Figure 1C*. We adopted a fiber-based Michelson interferometer, which provides flexibility in sample arm design and simplifies optical alignment. The design of the reference arm, the spectrometer, and the filtering optics of the light source resemble those in our previously reported system (31,32). Briefly, the interferometer used a 75:25 single-mode fiber coupler (Nufern 460-HP, Gould Fiber Optics), where 75% of the output light was directed to the reference while 25% was directed to the sample arm. A home-built spectrometer used an 1,800 lines per mm grating placed at the Littrow configuration of 28.6° (WP-1800/532, Wasatch Photonics) to disperse the light; a camera lens (Samyang 85 mm f/1.4) focused the light onto a linear CCD camera (spL2048-140 km, Basler). The magnification of the spectrometer was 2, providing a beam size of 7 μm on the camera, which is less than the pixel size of 10 μm .

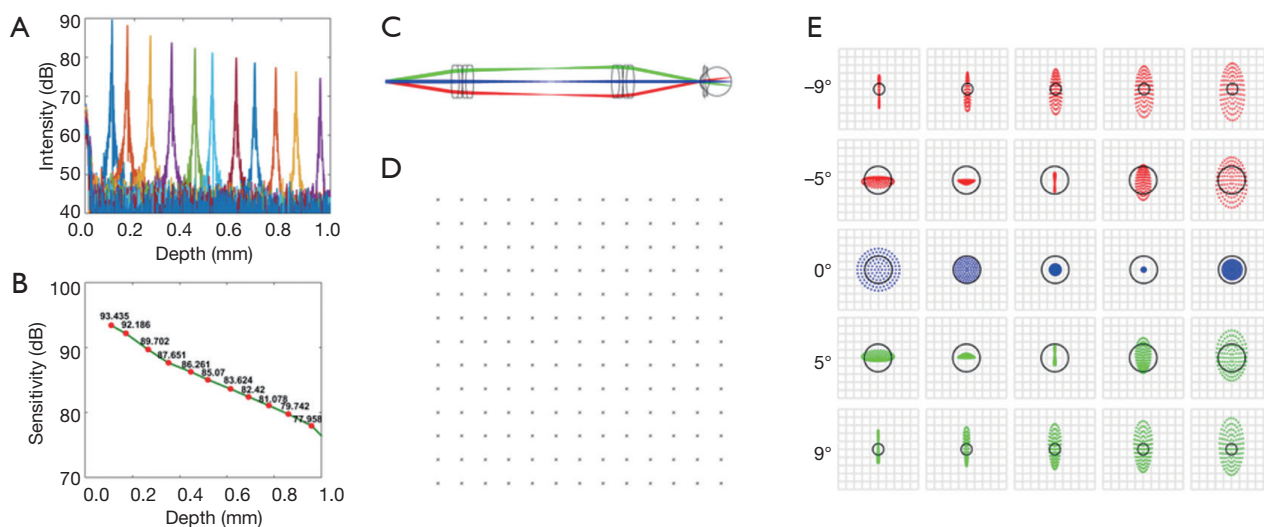


Figure 2 Characterization of the vis-OCT ophthalmoscope. (A) Measurements of system roll-off. (B) Measurements of system sensitivity. (C) Zemax schematic of the compound lens based telescopic system. Each compound lens consists of two achromatic doublets. The effective focal lengths of these lenses are 61 and 49 mm, respectively. Different colors represent scanning directions. (D) Zemax simulation showing grid distortion of an 18 degree square field of view on the retina centered at 0 degrees. (E) Zemax simulation of spot diagrams of the illumination light on retina. The three rows represent different scanning angles. First row: -9 degree; second row: -5 degree; Third row: 0 degree; Forth row: $+5$ degrees; Fifth row: $+9$ degrees. The horizontal positions from left to right represent relative depth: -150 , -75 , 0, 75 and 150 μm . The black circle in each spot diagram shows the airy disk. Vis-OCT, visible-light optical coherence tomography.

Figure 2 shows the experimental quantification of the system roll-off and Figure 2B shows the system sensitivity values at different depths. From Figure 2A, we measured that the roll-off of our vis-OCT system is 15 dB/mm. Because the retina is usually placed at the 200- μm location or closer with respect to zero delay position, system sensitivity was measured to be ~ 92 dB with 230 μW incident power. Beam diameter was 1.9 mm on the cornea, providing a diffraction limited beam size of 7.6 μm on the retina. Incorporating aberrations from the OpticStudio model of the human eye, OpticStudio calculations found that the lateral resolution of the system was around 10.2 μm at the center of the field of view and 12.5 μm at the ± 9 degree location in the retina. Theoretical axial resolution was calculated to be 1.4 μm in air and 1.1 μm in tissue (assuming a refractive index of 1.33). The measured axial resolution was 1.7 μm in air and 1.3 μm in tissue.

We significantly modified the sample arm to fit in a small housing mounted on a joystick base for both vertical and horizontal translations during alignment, as shown in Figure 3. The core components of the sample arm are two galvanometer mirrors and a pair of telescopic lenses that relay the scanning illumination beam to the pupil. The cart beneath the computer monitor houses the remaining optical

components, electronics, and light source on three shelves, out of sight (Figure 1C). The optical components include the reference arm and spectrometer, while the electronics include the power supply box for the galvanometer scanner, DAQ extension box, and shutter control unit.

We added three new features to improve the system performance. First, a dichroic mirror (DM in Figure 3) was added between the two telescopic lenses and a camera in the sample arm to enable pupil monitoring. As shown in Figure 3, the illumination light from two NIR (780 nm) LEDs mounted around the eyepiece is reflected by the pupil of the examined eye and transmits through the eyepiece, the dichroic mirror and a focusing lens. An integrated chip camera (generic-brand 1080 P AHD CCTV camera) generates an image of the pupil, which provides real-time guidance of the vis-OCT illumination. Previous iterations of the vis-OCT system required two users: one to position the patient's eye relative to the incident beam and another to control the computer. Adding the pupil monitoring enables a single photographer to image patients.

Second, the galvanometer scanner and its neighboring components, including one of the telescopic lenses and a reflection mirror, were mounted on a motorized stage (X-LRM050A, Zaber Technologies, Vancouver Canada),

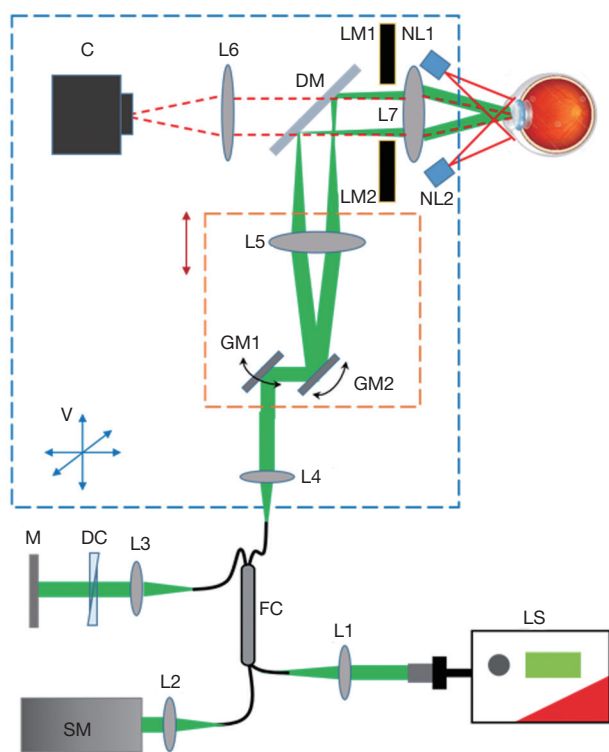


Figure 3 Vis-OCT ophthalmoscope schematic, including vis-OCT and pupil monitoring system. DM reflects visible light and transmits NIR light. The blue dashed square represents the aluminum box, which can be translated in 3D as shown by the blue arrows. V indicates vertical direction. The red dashed square represents the motorized stage, which can be translated vertically. LS, light source; FC, fiber coupler; DC, dispersion compensation; M, mirror; SM, spectrometer; GM1-2, galvanometer mirrors; L1-7, lenses; NR1-2, NIR LEDs; LM1-2, LED matrices for eye fixation; DM, dichroic mirror; C, camera; vis-OCT, visible-light optical coherence tomography; NIR, near-infrared.

which can be translated to adjust the divergence of the illuminating beam to correct for refractive error of the target eye. The benefit of translating the galvanometer scanner together with the telescopic lens is that the conjugate plane of the scanner, at which the illumination beam should enter the pupil, remained unchanged.

Third, in order to reduce the aberration of the illumination optics, we used compound lenses in the telescope relaying system. We used OpticStudio (Zemax, LLC) to simulate the performance of the illumination optics, determining the best commercially available lenses to use as well as the relative placement of the lenses. In order to minimize both chromatic and spherical aberrations,

we used two pairs of doublet lenses, as shown in *Figure 2C* (L5: Edmund Optics #47-642, 25 mm diameter \times 125 mm focal length achromatic doublet; L7: Edmund Optics #32-327, 25 mm diameter \times 100 mm focal length achromatic doublet). The grid distortion plot and spot diagrams of the final system are shown in *Figure 2D,E*. No discernible grid distortion is obvious within a ± 9 degree field of view. In the built-in OpticStudio model of the human eye, the field of view of ± 9 degrees corresponds to ± 3 mm as implemented in our system. OpticStudio modeling additionally allowed better estimation of the scanning range in the retina corresponding to measured angular scanning range that was limited by the NA of the L7 in *Figure 3*. More accurate knowledge of the actual scanning range in the retina can facilitate better selection of the region of interest and more accurate interpretation of the vis-OCT images.

Control software

We implemented the vis-OCT control software in LabVIEW (National Instruments, Austin, TX, USA). To improve programming efficiency and system reliability, we incorporated the state machine architecture and master/slave design pattern. We created a state machine for each relatively independent acquisition or processing task in the software, where the task was separated into a finite number of states. The transition between states depended on external user input or internal calculation. The state machine architecture led to a well-organized software structure and made it convenient to incorporate new functionalities. We also used master/slave design pattern. In brief, a master loop runs continuously in the background, sending commands to a series of slave loops, which may or may not be enabled based on the received commands. The flexibility of this design allows for the execution of multiple procedures either sequentially or in parallel depending on the situation.

The schematic of the overall software design is shown in *Figure 4*. The operation of the ophthalmoscope system requires four types of controls which are imaging control, stepper motor control, light source control, and 2D camera control. Imaging control is the core function of the software, which mostly involves programming and synchronization of a DAQ board (PCIe-6363, National Instruments) and a frame grabber (PCIe-1473, National Instruments). The DAQ board generated analog signals to deflect the voltage-driven galvanometer scanner and sent trigger signals to the frame grabber. Connected to

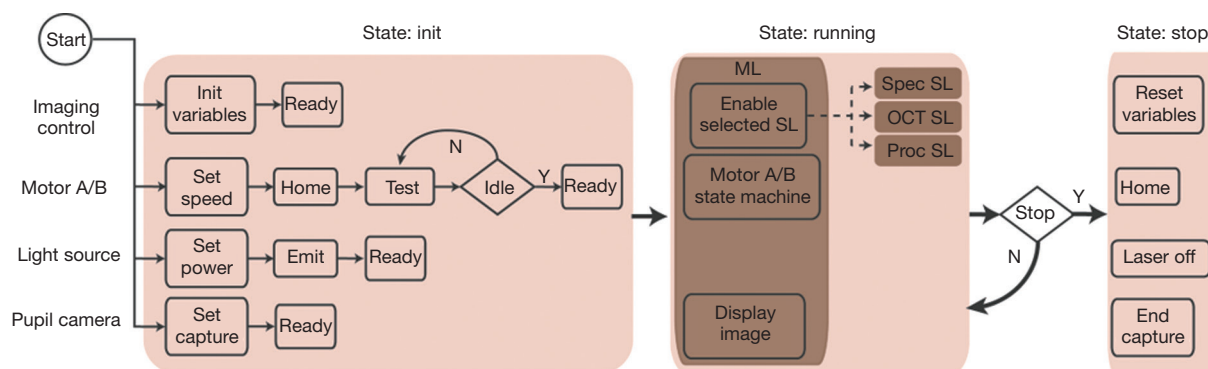


Figure 4 Flowchart of the system control software. Imaging control includes programming and synchronization of PCIe based DAQ board and camera link frame grabber. Two stepper motor based translation stages have the same control flowchart. In “Home” process, the stepper motor receives the command to find the “zero” position according to the built-in limit switch. In “Test” process, the program constantly queries the status of the motor until receiving an “Idle” signal, which indicates that the stage finishes translation and is ready for next command. This is function is designed for spectrometer alignment and system debugging by system engineers and inaccessible for clinical imaging technicians. All the slave loops also use state machine architecture. ML, master loop; Spec SL, the slave loop for displaying spectral interferogram in real time; OCT SL, the slave loop for OCT acquisition; Proc SL, the slave loop for offline OCT image reconstruction and processing; OCT, optical coherence tomography.

the spectrometer by two MDR (standard) to SDR (mini) Camera Link cables, the frame grabber acquired and stored spectral interferogram for image reconstruction. We sent serial commands via USB cables to control the stepper motor based translation stages for focus adjustment in the sample arm and imaging depth adjustment in the reference arm. We also used USB serial commands to control the switching and power level of the light source and the display of the pupil image by the 2D camera. We split the control flow chart into three states: *Init*, *Running*, and *Stop*. In the *Init* state, we initialized all the controlled entities. Upon receiving “Ready” signals from all the entities, the program entered the *Running* state, implemented with a master/slave design pattern. The master loop controlled the stepper motors and displayed the pupil image continuously while determining which slave loops to enable based on user input. The slave loops realized different functions in image acquisition and processing. New imaging modes can be easily added by inserting additional slave loops. All the slave loops also used state machine based architecture. The *Running* state continually recurs until the user closes the program and the program enters *Stop* state, where all tasks are terminated and cleared.

Eye fixation

Most laser scanning ophthalmic devices require eye

fixation to locate the region-of-interest (ROI) on the retina while minimizing motion during image acquisition. The ophthalmoscopes using NIR light sources normally use internal fixation, where the invisible illumination light is combined with a controlled visible light fixation target by a dichroic mirror inside the imaging system. Patients are instructed to focus on the visible fixation target during imaging sessions. The position of the fixation target can be manipulated to position ROI.

Eye fixation in vis-OCT imaging is more challenging. The probing light for vis-OCT can overshadow a visible fixation target and induce additional eye motion, as illustrated in *Figure 5A*. Therefore, we adopted an external fixation method. We mounted an LED array behind the eyepiece, where only one element is turned on during image acquisition. The non-imaged eye (fellow eye) of the patient looked at the lit-up LED element while the imaged eye was being scanned, as shown in *Figure 5B*. To image different ROIs such optic nerve head (ONF) or macular regions, we changed the position of the lit-up LED on the array.

Imaging protocol

We designed three protocols for human eye imaging by vis-OCT: *raster preview*, *raster acquisition*, and *circular acquisition*. For all the protocols, the A-line acquisition rate was 25 kHz and the illumination power on the cornea was kept under

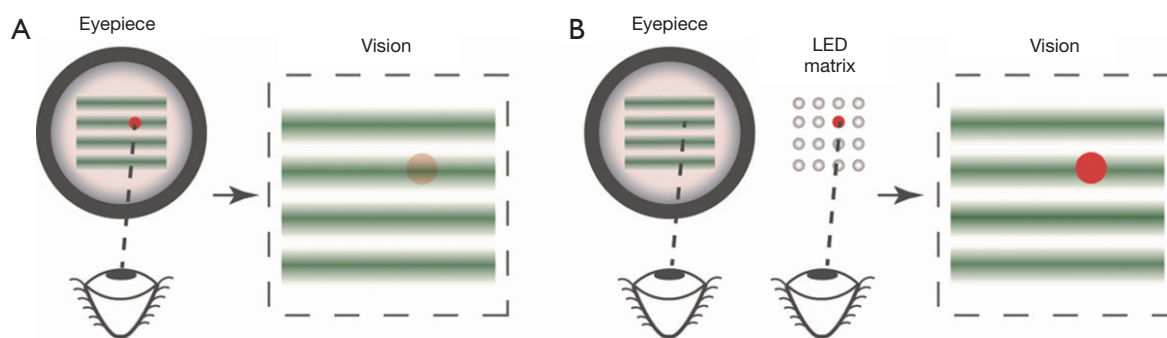


Figure 5 (A) Internal and (B) external fixation in retinal imaging by vis-OCT. Vis-OCT, visible-light optical coherence tomography.

250 μ W, which is within the maximum permissible exposure (MPE) defined by the American National Standard for Safe Use of Lasers (ANSI Z136.1-2014) (17,31,34).

Raster preview enabled a real-time, live display for alignment purposes. In this mode, we took low-density vis-OCT images (256 \times 16 A-lines) continuously, covering a squared area of 7 \times 7 mm² on the retina. We displayed one of the sixteen B-scans together with an *en face* maximum projection along the axial direction. Image reconstruction was accelerated by CUDA parallel computation based on GPU. The acquisition rate was 5 frames per second (FPS), which, though limited by the A-line number and spectrometer integration time, was sufficient to guide the operator in real time to optimize illumination focus and to locate ROI. On average, an operator with basic training required around 20 seconds to detect the retina by translating the reference mirror, another 20 seconds to locate the ROI by controlling LED array, and a further 5 seconds to optimize focus by adjusting the distance between two telescopic lenses in the sample arm. The total alignment time has been shown to be around 1 minute.

In *raster acquisition*, we took a high-density vis-OCT image (512 \times 256 A-lines), covering the same ROI as the *raster preview* protocol. It took 5.2 seconds to complete the high-density image acquisition. In *circular acquisition*, 16 repeated circular B-scans, each consisting of 4,096 A-lines, were taken along a 5-mm diameter ring on the retina centered on the same region as the raster scan protocols. The circular scan image acquisition time was 2.6 seconds. We saved the OCT data acquired by the two acquisition protocols on the local hard drive.

Following either acquisition mode, a pop-up window queries whether the user would like to process the data. If the “yes” option is selected, the program requires about 15 seconds to process and display the *en face* data. At that point,

the user can click and drag a line crossing the *en face* image to view the B-scan corresponding to that line.

For safety reason we placed software controlled mechanical shutter (LS6, Vincent Associated, Rochester, NY, USA) at the interferometer input to prevent any damage to the patient’s eye. In case of any errors in the software the shutter was automatically closed.

Results

We imaged both healthy and diseased human eyes using vis-OCT to evaluate its suitability for the next-stage clinical studies.

Vis-OCT imaging of healthy subject

Figure 6 shows vis-OCT images from a healthy subject (24-year-old). We imaged regions around both the macula and the ONH. The macula is responsible for the sharp central vision of the human eye. Compared to the area around the ONH, the macula shows a thinner RNFL as well as reduced vessel size and density. The fovea, the avascular zone at the center of the macula, appears as a darker area in the *en face* image shown in *Figure 6A* due to lack of RNFL and its strong backscattering signal. *Figure 6B* shows a typical B-scan of the macula, whose different anatomical layers can be clearly resolved. A normalized A-line is shown in *Figure 6C*. The features of vis-OCT can be better demonstrated by the images of the region around the ONH, where major retina arteries and veins arise, as shown in *Figure 6D*. The axons of retinal ganglion cells also gather at ONH, leading to increased RNFL thickness. The B-scan in *Figure 6E* demonstrates high contrast in visualizing the RNFL and the outer retinal layers. The outer retinal layers are defined here as being the

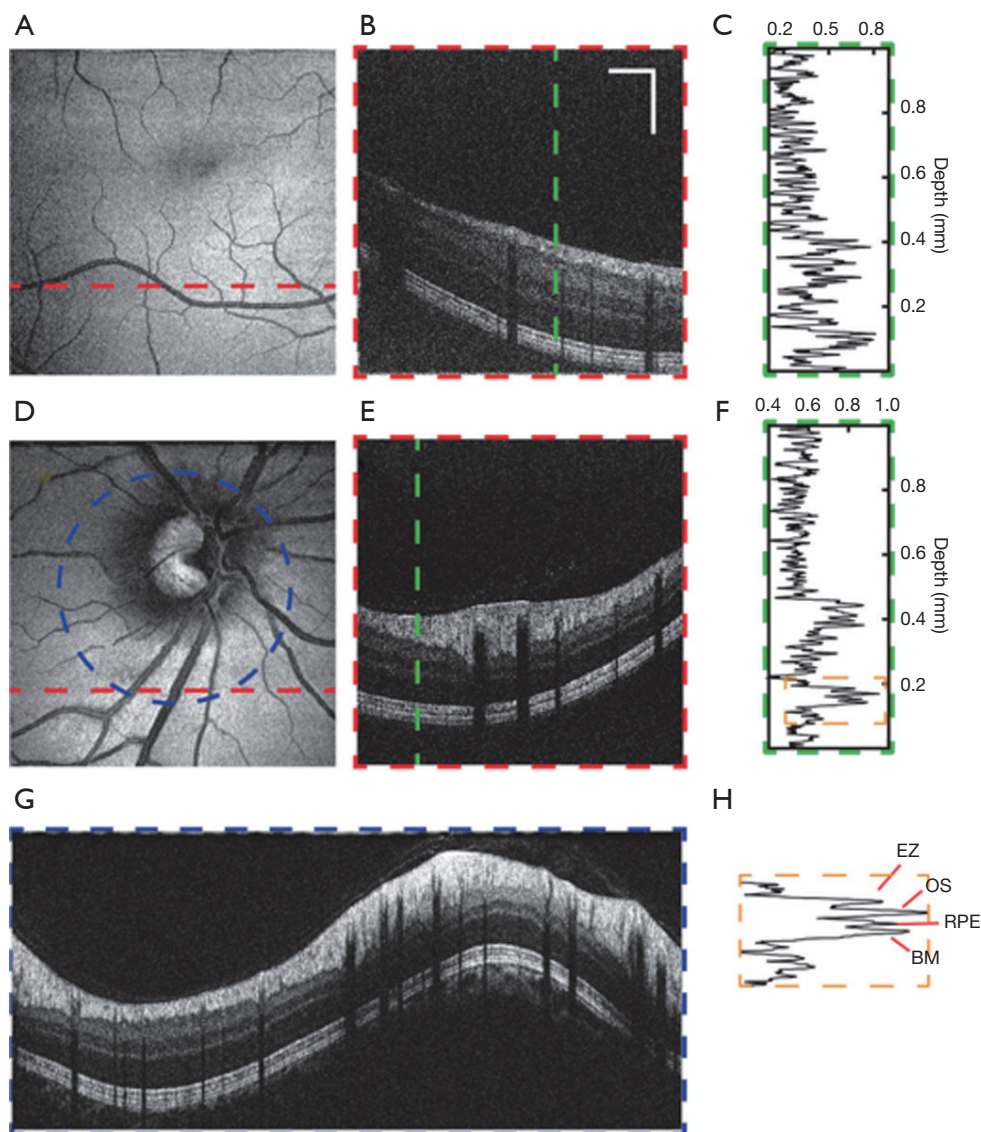


Figure 6 Vis-OCT images of a healthy eye. (A-C) Images of macula. (A) *En face* image. (B) The B-scan along the red dashed line in (A). (C) The A-line along the green dashed line in (B). (D-G) Images of the retina around optic nerve head (ONH). (D) *En face* image. (E) The B-scan along the red dashed line in (D). (F) The A-line along the green dashed line in (E). (G) The circular B-scan along the blue dashed line in (D). (H) Zoom-in of the section outlined with orange box from (F) with each of the four layers labelled: EZ, OS, RPE, BM. Scale bar, 1 mm (lateral) by 0.2 mm (axial). No image averaging. EZ, ellipsoid zone; OS, outer segments of photoreceptors; RPE, retinal pigment epithelium; BM, Bruch's membrane; vis-OCT, visible-light optical coherence tomography.

layers beneath the outer limiting membrane (OLM). The normalized A-line shown in *Figure 6F* also suggests that vis-OCT has stronger signal from the RNFL as well as the outer retinal layers, while the layers between the RNFL and OLM show weaker signal. It also demonstrates the high axial resolution of vis-OCT, indicated by the four clearly separated peaks in the outer retina corresponding to the

boundary between photoreceptor inner and outer segments (also known as the ellipsoid zone or EZ), the outer segment of photoreceptors (OS), retinal pigment epithelium (RPE), and Bruch's membrane (BM), as can be seen in *Figure 6H*. However, unlike NIR-OCT, which can penetrate into the choroid, vis-OCT can barely image anything beyond the BM due to strong attenuation of visible light by the RPE.

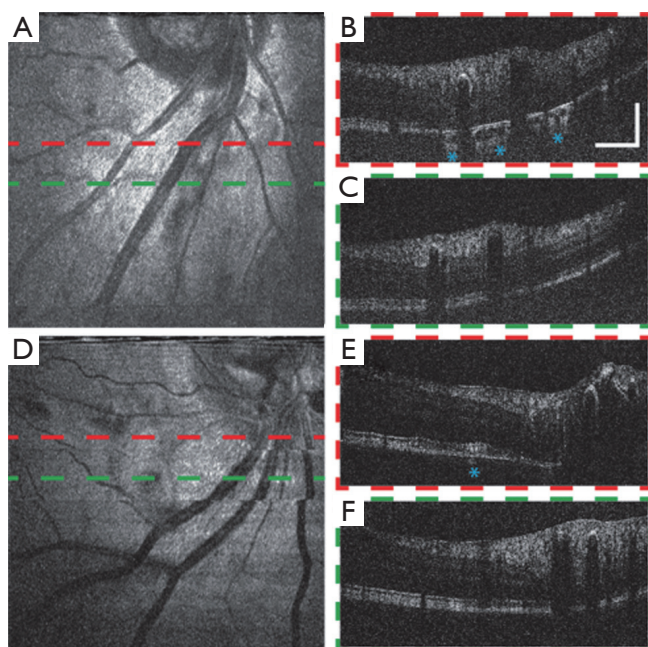


Figure 7 Vis-OCT images of eyes with ocular vascular occlusive diseases. (A)-(C) Images of a patient (79-year-old) with central retinal artery occlusion (CRAO). (A) *En face* image of the region below ONH. (B) B-scan along the red dashed line in (A). (C) B-scan along the green dashed line in (A). (D-F) Images of a patient (49-year-old) with CRAO. (D) *En face* image of the region below ONH. (E) B-scan along the red dashed line in (D). (F) B-scan along the green dashed line in (D). Scale bar, 1 mm (lateral) by 0.2 mm (axial). Blue asterisks: areas where the choroid can be seen. No image averaging. Vis-OCT, visible-light optical coherence tomography; ONH, optic nerve head.

A circular scan around the ONH with a higher sampling density is shown in *Figure 6G*, in which the major retinal blood vessels can be identified.

Vis-OCT imaging of patients with retinal occlusive diseases

We show vis-OCT retinal images of patients with ocular vascular occlusive diseases, a family of diseases representing a common cause of visual disability (37), in *Figure 7*. Occlusions in retinal blood vessels lead to hemodynamic insufficiency, whose pathology can potentially be studied by functional vis-OCT. *Figure 7A* shows an *en face* image from a patient (79-year-old) with central retinal artery occlusion (CRAO). Typical B-scan images are shown in *Figure 7B,C*. Compared with those of young healthy subjects, these images exhibit less contrast between different retinal layers

and weaker signal intensity compared with noise level in the background due to age- and disease-related reduction of the eye's optical quality. .

The B-scan image in *Figure 7B* shows that the illumination light penetrates into the choroid at certain regions as highlighted by the asterisks. We hypothesize that such increased penetration of light into the choroid is due to the loss of RPE cells or RPE melanin, which requires further investigation. *Figure 7D,E,F* show images of another CRAO patient (49-year-old) having similar features with the previous case. Though without significant observed RPE loss, the outer retinal layers of this subject have uneven cross-section and inhomogeneous signal intensity distribution, which may be a complication of CRAO. We also highlight a region where light penetrates the choroid in *Figure 7E*.

Vis-OCT imaging of patients with DR

Figure 8 shows vis-OCT images of patients with DR, which is the leading cause of blindness in the working-age population in the United States (38). Preliminary studies in an animal model suggested that vis-OCT has the potential to improve clinical management of DR (29). *Figure 8A,B,C,D* show the images around the ONH from a DR patient (57-year-old). Minor motion artifacts exist in the *en face* image, since visual impairment in the patient's fellow eye influence effective external fixation. The circular B-scan provides stronger contrast and better image quality than normal B-scans due to higher sampling density. Multiple hyper-reflective points distributed around the retina highlight the leaky blood vessels and intraretinal fluid. An epiretinal membrane is formed on the surface of the inner retina (39). Some backscattering signals from the choroid can be visualized, indicating less melanin in the RPE than in the young healthy subject. *Figure 8E,F,G* show the images of a second DR patient (38-year-old). Besides similar features with the previous case, this subject has severe retinal edema indicated by abnormally thickened retina and detachment of epiretinal membrane. Minimal signal from the choroid suggest higher RPE melanin concentration, which can be expected due to the patient's young age.

Discussion

We developed a vis-OCT imaging platform for human retinal imaging. We translated our previous laboratory-based prototype to an integrated, compact ophthalmoscope,

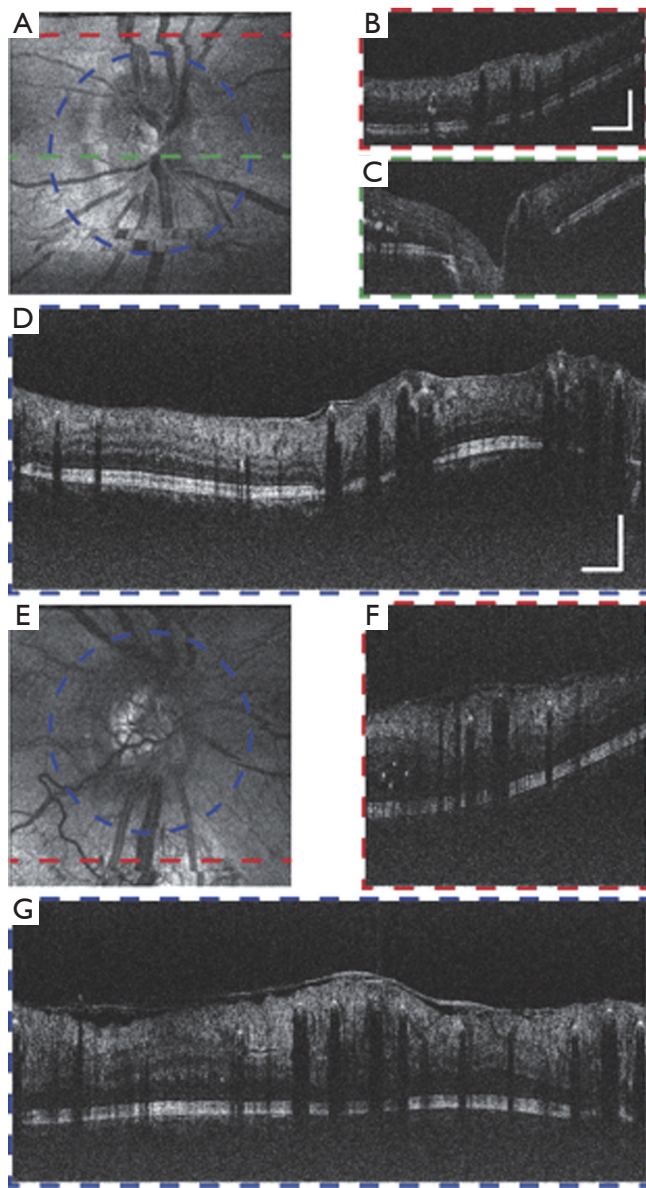


Figure 8 Vis-OCT images of eyes with diabetic retinopathy (DR). (A,B,C,D) Images of a DR patient (57-year-old) (A) *En face* image of the region around ONH. (B) B-scan image along the red dashed-line in (A). Scale bar: 1 mm (lateral) by 0.2 mm (axial), applies to (A,B,C). (C) B-scan image along the green dashed-line in (A). (D) Circular B-scan image along the blue dashed-line in (A). Scale bar: 1 mm (lateral) by 0.2 mm (axial), applies to (D,E,F,G). (E,F,G) Images of another DR patient (38-year-old). (E) *En face* image of the region around ONH. (F) B-scan image along the red dashed-line in (E). (G) Circular B-scan image along the blue dashed-line in (E). No image averaging. Vis-OCT, visible-light optical coherence tomography; ONH, optic nerve head.

whose appearance and operation closely resembled commercial ophthalmic OCTs. We tested this newly-designed system in human subjects with both healthy and diseased eyes.

We demonstrate the feasibility of vis-OCT in imaging elderly individuals with common ocular diseases. Previous studies only focused on young healthy volunteers with good eye conditions (31-33). It remained unclear whether vis-OCT can image patients, whose eyes may have much lower transmittance to visible light due to aging or diseases. In this study, we imaged patients across a broad range of ages using vis-OCT ophthalmoscope. We acquired images with good quality while limiting the illumination power within 20% of the MPE defined by ANSI. Although only the patients with retinal occlusive diseases and DR are imaged in this study, we expect that vis-OCT can also be used to image individuals with other diseases.

We show the characteristics of vis-OCT in retinal imaging. The shorter illumination wavelengths lead to increased scattering from RNFL and stronger attenuation in the RPE. Therefore, vis-OCT images have relatively higher signal intensity in the RNFL but barely provide any information in the choroid. The axial resolution of vis-OCT, proportional to the square of center illumination wavelength, is also higher than NIR-OCT using comparable bandwidth. Lateral resolution also increases, although only linearly, with decreasing wavelength. We show that vis-OCT provided a good visualization of the outer retinal layers, especially the boundary between RPE and BM without any averaging.

Vis-OCT has the potential to be applied to various eye diseases. Due to improved imaging contrast in the RNFL and higher axial resolution, vis-OCT might be more suitable to measure RNFL morphological changes, which are associated with the progression of glaucoma (40). Since the RPE melanin is the major absorber of visible illumination light, reduced melanin concentration or complete loss of RPE cells gives rise to choroid signals in vis-OCT images, which cannot be observed otherwise. Therefore, vis-OCT might be better suited than NIR-OCT in studying alterations in melanin concentration in the RPE, which is both a risk factor and early symptom of AMD (41,42).

Using spectroscopic analysis, vis-OCT has the potential to study hemodynamic variations associated with various retinal diseases. Quantitative retinal metabolic measurements in rodent model by vis-OCT using

spectroscopic and Doppler analysis have revealed pathology of different retinal diseases (13,29,30). After demonstrating the extraction of functional information from vis-OCT images and the feasibility of routine clinical imaging, our next goal is to study disease related hemodynamic variations in patients.

Compared with the state-of-the-art commercial OCTs using NIR light, vis-OCT has several limitations. First, visible light scanning is distracting and overshadows the internal fixation target, leading to stronger eye motion. We used external fellow eye fixation, which is an effective way to minimize motion artifacts as suggested by our imaging results. Second, imaging sensitivity of vis-OCT is currently lower than that of NIR-OCT due to lower illumination power for safety and comfort concerns and greater noise from the SC light source (17,33). Therefore, the imaging speed of vis-OCT is slower than that of commercial NIR OCT systems to compensate for the lower SNR. Developing new broadband light sources between 500 and 600 nm with minimal relative intensity noise can significantly improve the performance of vis-OCT, improve the accuracy of quantitative metabolic measurement, and facilitate vis-OCT's clinical translations.

Conclusions

In summary, we developed a portable vis-OCT system and tested its applicability towards imaging in patients with decreased ability to concentrate on target in clinical setting. The new system provides improved-quality images in both individuals without known eye diseases and patients with retinal occlusive diseases and DR. This newly developed system sets the stage to large-scale clinical studies in order to establish the clinical impact of vis-OCT.

Acknowledgments

Funding: This work was supported in part by the National Institute of Health grants DP3DK108248, R01EY026078, R01EY029121, R01EY028304, R44EY026466, and R43EY028475.

Footnote

Conflicts of Interest: JS Schuman and HF Zhang have financial interests in Opticent Health. Y Wang is a full-time employee of Opticent Health. R Kuranov is a part-time

employee of Opticent Health. The other authors have no conflicts of interest to declare.

Ethical Statement: The study was approved by the Northwestern University Institutional Review Board and written informed consent was obtained from all patients.

References

- Huang D, Swanson EA, Lin CP, Schuman JS, Stinson WG, Chang W, Hee MR, Flotte T, Gregory K, Puliafito CA. Optical coherence tomography. *Science* 1991;254:1178-81.
- Schmitt JM. Optical coherence tomography (OCT): a review. *IEEE J Sel Top Quantum Electron* 1999;5:1205-15.
- Drexler W, Fujimoto JG. *Optical coherence tomography: technology and applications*. Springer 2015.
- Leitgeb RA, Werkmeister RM, Blatter C, Schmetterer L. Doppler optical coherence tomography. *Prog Retin Eye Res* 2014;41:26-43.
- Chen Z, Zhang J. Doppler optical coherence tomography. *Optical Coherence Tomography: Technology and Applications* 2015:1289-320.
- Shu X, Liu W, Duan L, Zhang HF. Spectroscopic Doppler analysis for visible-light optical coherence tomography. *J Biomed Opt* 2017;22:1-8.
- de Boer JF, Milner TE. Review of polarization sensitive optical coherence tomography and Stokes vector determination. *J Biomed Opt* 2002;7:359-71.
- Pircher M, Hitzinger CK, Schmidt-Erfurth U. Polarization sensitive optical coherence tomography in the human eye. *Prog Retin Eye Res* 2011;30:431-51.
- Jia Y, Bailey ST, Hwang TS, McClintic SM, Gao SS, Pennesi ME, Flaxel CJ, Lauer AK, Wilson DJ, Hornegger J. Quantitative optical coherence tomography angiography of vascular abnormalities in the living human eye. *Proc Natl Acad Sci U S A* 2015;112:E2395-402.
- Liu W, Li H, Shah RS, Shu X, Linsenmeier RA, Fawzi AA, Zhang HF. Simultaneous optical coherence tomography angiography and fluorescein angiography in rodents with normal retina and laser-induced choroidal neovascularization. *Opt Lett* 2015;40:5782-5.
- Kashani AH, Chen CL, Gahm JK, Zheng F, Richter GM, Rosenfeld PJ, Shi Y, Wang RK. Optical coherence tomography angiography: A comprehensive review of current methods and clinical applications. *Prog Retin Eye Res* 2017;60:66-100.
- Zhang X, Hu J, Knighton RW, Huang XR, Puliafito CA,

- Jiao S. Dual-band spectral-domain optical coherence tomography for in vivo imaging the spectral contrasts of the retinal nerve fiber layer. *Opt Express* 2011;19:19653-9.
13. Yi J, Liu W, Chen S, Backman V, Sheibani N, Sorenson CM, Fawzi AA, Linsenmeier RA, Zhang HF. Visible light optical coherence tomography measures retinal oxygen metabolic response to systemic oxygenation. *Light Sci Appl* 2015;4.
 14. Lichtenegger A, Harper DJ, Augustin M, Eugui P, Muck M, Gesperger J, Hitzemberger CK, Woehrer A, Baumann B. Spectroscopic imaging with spectral domain visible light optical coherence microscopy in Alzheimer's disease brain samples. *Biomed Opt Express* 2017;8:4007-25.
 15. Považay B, Apolonski A, Unterhuber A, Hermann B, Bizheva KK, Sattmann H, Russell PSJ, Krausz F, Fercher AF, Drexler W. editors. Visible light optical coherence tomography. *Proc SPIE* 2002.
 16. Robles FE, Wilson C, Grant G, Wax A. Molecular imaging true-colour spectroscopic optical coherence tomography. *Nat Photonics* 2011;5:744-7.
 17. Shu X, Beckmann LJ, Zhang HF. Visible-light optical coherence tomography: a review. *J Biomed Opt* 2017;22:1-14.
 18. Chen S, Shu X, Yi J, Fawzi A, Zhang HF. Dual-band optical coherence tomography using a single supercontinuum laser source. *J Biomed Opt* 2016;21:66013.
 19. Bizheva K, Tan B, MacLellan B, Kralj O, Hajialamdari M, Hileeto D, Sorbara L. Sub-micrometer axial resolution OCT for in-vivo imaging of the cellular structure of healthy and keratoconic human corneas. *Biomed Opt Express* 2017;8:800-12.
 20. Duan L, McRaven MD, Liu W, Shu X, Hu J, Sun C, Veazey RS, Hope TJ, Zhang HF. Colposcopic imaging using visible-light optical coherence tomography. *J Biomed Opt* 2017;22:56003.
 21. Chong SP, Merkle CW, Leahy C, Radhakrishnan H, Srinivasan VJ. Quantitative microvascular hemoglobin mapping using visible light spectroscopic Optical Coherence Tomography. *Biomed Opt Express* 2015;6:1429-50.
 22. Chen S, Yi J, Liu W, Backman V, Zhang HF. Monte Carlo investigation of optical coherence tomography retinal oximetry. *IEEE Trans Biomed Eng* 2015;62:2308-15.
 23. Song W, Wei Q, Liu W, Liu T, Yi J, Sheibani N, Fawzi AA, Linsenmeier RA, Jiao S, Zhang HF. A combined method to quantify the retinal metabolic rate of oxygen using photoacoustic ophthalmoscopy and optical coherence tomography. *Sci Rep* 2014;4:6525.
 24. Pi S, Camino A, Cepurna W, Wei X, Zhang M, Huang D, Morrison J, Jia Y. Automated spectroscopic retinal oximetry with visible-light optical coherence tomography. *Biomed Opt Express* 2018;9:2056-67.
 25. Linsenmeier RA, Zhang HF. Retinal oxygen: from animals to humans. *Prog Retin Eye Res* 2017;58:115-51.
 26. Jacques SL. Optical properties of biological tissues: a review. *Phys Med Biol* 2013;58:R37.
 27. Huang XR, Zhou Y, Kong W, Knighton RW. Reflectance decreases before thickness changes in the retinal nerve fiber layer in glaucomatous retinas. *Invest Ophthalmol Vis Sci* 2011;52:6737-42.
 28. Yi J, Puyang Z, Feng L, Duan L, Liang P, Backman V, Liu X, Zhang HF. Optical Detection of Early Damage in Retinal Ganglion Cells in a Mouse Model of Partial Optic Nerve Crush Injury Early Detection of RGC Damages. *Invest Ophthalmol Vis Sci* 2016;57:5665-71.
 29. Liu W, Wang S, Soetikno B, Yi J, Zhang K, Chen S, Linsenmeier RA, Sorenson CM, Sheibani N, Zhang HF. Increased Retinal Oxygen Metabolism Precedes Microvascular Alterations in Type 1 Diabetic Mice Retinal Oxygen Consumption Increases in Diabetic Mice. *Invest Ophthalmol Vis Sci* 2017;58:981-9.
 30. Soetikno BT, Yi J, Shah R, Liu W, Purta P, Zhang HF, Fawzi AA. Inner retinal oxygen metabolism in the 50/10 oxygen-induced retinopathy model. *Sci Rep* 2015;5:16752.
 31. Yi J, Chen S, Shu X, Fawzi AA, Zhang HF. Human retinal imaging using visible-light optical coherence tomography guided by scanning laser ophthalmoscopy. *Biomed Opt Express* 2015;6:3701-13.
 32. Chen S, Shu X, Nesper PL, Liu W, Fawzi AA, Zhang HF. Retinal oximetry in humans using visible-light optical coherence tomography. *Biomed Opt Express* 2017;8:1415-29.
 33. Chong SP, Bernucci M, Radhakrishnan H, Srinivasan VJ. Structural and functional human retinal imaging with a fiber-based visible light OCT ophthalmoscope. *Biomed Opt Express* 2016;8:323-37.
 34. Standard A. Z136. 1. American national standard for the safe use of lasers. New York: American National Standards Institute. Inc., 2014.
 35. Kessel L, Lundeman JH, Herbst K, Andersen TV, Larsen M. Age-related changes in the transmission properties of the human lens and their relevance to circadian entrainment. *J Cataract Refract Surg* 2010;36:308-12.
 36. Beems EM, Van Best JA. Light transmission of the cornea in whole human eyes. *Exp Eye Res* 1990;50:393-5.

37. Hayreh SS. Prevalent misconceptions about acute retinal vascular occlusive disorders. *Prog Retin Eye Res* 2005;24:493-519.
38. Mohamed Q, Gillies MC, Wong TY. Management of diabetic retinopathy: a systematic review. *JAMA* 2007;298:902-16.
39. Trichonas G, Kaiser PK. Optical coherence tomography imaging of macular oedema. *Br J Ophthalmol* 2014;98:ii24-9.
40. Dong ZM, Wollstein G, Wang B, Schuman JS. Adaptive optics optical coherence tomography in glaucoma. *Prog Retin Eye Res* 2017;57:76-88.
41. Shu X, Li H, Dong B, Sun C, Zhang HF. Quantifying melanin concentration in retinal pigment epithelium using broadband photoacoustic microscopy. *Biomed Opt Express* 2017;8:2851-65.
42. Boulton M. Ageing of the retina and retinal pigment epithelium. *Age-Related Macular Degeneration*. Springer 2013:45-63.

Cite this article as: Shu X, Beckmann L, Wang Y, Rubinoff I, Lucy K, Ishikawa H, Wollstein G, Fawzi AA, Schuman JS, Kuranov RV, Zhang HF. Designing visible-light optical coherence tomography towards clinics. *Quant Imaging Med Surg* 2019;9(5):769-781. doi: 10.21037/qims.2019.05.01